Spatiotemporal evolution of cavitation dynamics exhibited by flowing microbubbles during ultrasound exposure

James J. Choi[a)] and Constantin-C. Coussios

Biomedical Ultrasonics, Biotherapy, and Biopharmaceuticals Laboratory, Institute of Biomedical Engineering, Department of Engineering Science, University of Oxford, Oxford, Oxfordshire OX3 7DQ, United Kingdom

Ultrasound and microbubble-based therapies utilize cavitation to generate bioeffects, yet cavitation dynamics during individual pulses and across consecutive pulses remain poorly understood under physiologically relevant flow conditions. SonoVue® microbubbles were made to flow (fluid velocity: 10–40 mm/s) through a vessel in a tissue-mimicking material and were exposed to ultrasound [frequency: 0.5 MHz, peak-rarefactional pressure (PRP): 150–1200 kPa, pulse length: 1–100 000 cycles, pulse repetition frequency (PRF): 1–50 Hz, number of pulses: 10–250]. Radiated emissions were captured on a linear array, and passive acoustic mapping was used to spatiotemporally resolve cavitation events. At low PRPs, stable cavitation was maintained throughout several pulses, thus generating a steady rise in energy with low upstream spatial bias within the focal volume. At high PRPs, inertial cavitation was concentrated in the first 6.3 ± 1.3 ms of a pulse, followed by an energy reduction and high upstream bias. Multiple pulses at PRFs below a flow-dependent critical rate ($\mathrm{PRF_{crit}}$) produced predictable and consistent cavitation dynamics. Above the $\mathrm{PRF_{crit}}$, energy generated was unpredictable and spatially biased. In conclusion, key parameters in microbubble-seeded flow conditions were matched with specific types, magnitudes, distributions, and durations of cavitation; this may help in understanding empirically observed *in vivo* phenomena and guide future pulse sequence designs. © *2012 Acoustical Society of America.*
[http://dx.doi.org/10.1121/1.4756926]

I. INTRODUCTION

Focused ultrasound (FUS) in conjunction with pre-formed microbubbles is being developed for a wide range of therapeutic applications. Microbubbles, which are typically administered systemically and therefore remain within the vasculature, are employed as acoustic cavitation seeds and promoters that interact with the luminal contents or the vascular wall. Depending on the driving acoustic pulse sequence, the microbubble composition and distribution, and vascular network targeted, a diverse range of biological outcomes can be realized (Coussios and Roy, 2008). In drug delivery, vessel-contained cavitation activity can increase vascular permeability for enhanced molecular and nanoparticle extravasation (e.g., blood-brain barrier disruption, tumor viral delivery, drug delivery to the heart, etc.) (Arvanitis *et al.*, 2011; Bazan-Peregrino *et al.*, 2012; Bekeredjian *et al.*, 2005; Choi *et al.*, 2007; Hynynen *et al.*, 2001), fragmentation of the microbubble can release encapsulated drugs for targeted release (Ferrara *et al.*, 2007), and convection enhancement can facilitate molecular transport (Marmottant and Hilgen-feldt, 2003; Rifai *et al.*, 2010). Other microbubble-mediated therapies include dissolution of thrombi through mechanical disruption (Datta *et al.*, 2008; Datta *et al.*, 2006), molecular delivery to cells through sonoporation (Deng *et al.*, 2004), enhancement of renal ultrafiltration (Fischer *et al.*, 2009), and blood clotting through hemostasis (Poliachik *et al.*, 2001). Despite advances in the aforementioned techniques, both

their biological and cavitation mechanisms remain poorly understood and are in a large part due to limitations in the ability to control and monitor cavitation dynamics generated. The lack of mechanistic understanding and the limits to control and monitoring reinforce each other and impede development toward effective and safe microbubble-mediated therapies. Advances on both fronts could help enhance therapeutic effects while avoiding unintended damage, such as erythrocyte extravasation (Baseri *et al.*, 2010), and, in extreme situations, hemorrhage (Daffertshofer *et al.*, 2005).

A large body of work has investigated how the characteristics of an ultrasonic pulse waveform influence acoustic cavitation phenomena. At low peak rarefactional pressures (PRPs), microbubbles undergo stable radial oscillations that can last several acoustic cycles leading to the radiation of acoustic emissions rich in harmonics of the driving center frequency. At long pulse lengths (PLs), a microbubble can experience a net displacement away from the transducer due to radiation force effects and a change in its equilibrium radius due to rectified diffusion or gas leakage (Apfel, 1997). Stable cavitation occurring along the vascular wall can cause vessel expansion and contraction (Caskey *et al.*, 2007) in capillaries and have been proposed as a mechanism for the increase in vascular permeability (McDannold *et al.*, 2006; Tung *et al.*, 2010b). Escalation of the PRP amplifies the radial oscillations until unstable growth of the bubble occurs during the rarefactional pressure half-cycle, leading to a violent collapse dominated by the inertia of the surrounding medium that is accompanied by the radiation of broadband acoustic emissions. Inertial cavitation has been associated with numerous bioeffects ranging from

---

[a)]Author to whom correspondence should be addressed. Electronic mail: james.choi@eng.ox.ac.uk

molecular and cellular extravasations to vascular rupture (Chen *et al.*, 2011).

Microbubbles are the seed and promoters of cavitation events and are therefore the discrete sites of mechanical action within the vascular environment. Most of the desired bioeffects cannot occur without them. The most widely employed class of microbubbles is lipid-shelled with a stabilized gas core (e.g., Definity® and SonoVue®) and has been specifically designed to enhance image contrast and persistence timelines, which include robustness of structure, stealth from the immune system, and reduced renal clearance. However, in an acoustic field, microbubbles may be pushed away due to radiation force effects, trapped in acoustic nodes and anti-nodes, modulated in size and composition (growth or shrinkage), or destroyed due to fragmentation or inertial cavitation collapse (Ferrara *et al.*, 2007). All these effects coupled with a dynamic pulsatile flow environment with variable vessel sizes and boundary conditions, amount to a complex and changing acoustic cavitation behavior. Indeed, several studies have shown that a sufficient time interval between ultrasonic pulses is required to allow for unmodulated microbubbles to reperfuse the focused ultrasound targeted tissue volume to generate specific therapeutic outcomes (Caskey *et al.*, 2007; Choi *et al.*, 2011a; Goertz *et al.*, 2010; Hitchcock *et al.*, 2011; McDannold *et al.*, 2006; Samuel *et al.*, 2009a). Models for characterizing destruction-replenishment kinetics of microbubbles have been extensively studied for diagnostic perfusion imaging (Hudson *et al.*, 2009; Wei *et al.*, 1998) but have not yet been extended to therapeutic applications.

Understanding the spatiotemporal evolution of ultrasonically driven cavitation activity under flow conditions is critical for the optimization and monitoring of therapeutic applications and has been investigated using a wide range of techniques. Optical observations using high-speed cameras have provided direct measurements of the bubble radius during compressional and rarefactional phases in both static and flow environments (Caskey *et al.*, 2007; Chen *et al.*, 2011; Chomas *et al.*, 2001). However, optical observations are limited to single or a few microbubbles near the focal point and to a few cycles, whereas therapeutic applications typically sonicate a population of microbubbles for several milliseconds. Cavitation activity has also been monitored actively or passively using a single-element transducer confocally aligned with the therapeutic transducer. However, single-element detectors are limited to a single sensing volume and therefore provide no information as to the number or spatial distribution of cavitation events occurring outside of this volume or at best a one-dimensional representation of the location of cavitation events happening closest to the detecting transducer. A recently developed technique, known as passive acoustic mapping (PAM) enables the ability to locate and quantify cavitation activity during ultrasound exposure by sensing cavitation-generated acoustic emissions using an array of detectors (Gyöngy and Coussios, 2010a). PAM has been shown to track individual sites of cavitation activity with sub-millimeter spatial and millisecond temporal accuracy (Gyöngy and Coussios, 2010b) and has been used effectively to detect inertial cavitation events during high-intensity focused ultrasound exposure and predict lesion formation (Jensen *et al.*, 2012).

The purpose of this paper is to understand how microbubble-seeded cavitation dynamics spatiotemporally evolve during ultrasonic exposure in a flow environment. More specifically, it is assumed that upstream (i.e., arteries and arterioles) spatially biased therapeutic effects (Choi *et al.*, 2011a; Choi *et al.*, 2011b; Choi *et al.*, 2010) are caused by upstream spatially biased cavitation activity due to microbubble destruction-replenishment phenomena. It is subsequently hypothesized that flow-induced spatially biased cavitation activity can occur both through several pulses due to selection of the pulse repetition frequency (PRF) and within a single pulse due to selection of the PL. PAM was employed not only to track the spatial distribution of cavitation activity over time but also to classify the type and quantify the magnitude of cavitation generated. Analysis was performed during sonication to extract therapeutically relevant parameters (e.g., PRP, PL, and PRF) with respect to flow conditions. Insight gained from this fundamental investigation may help understand *in vivo* phenomena, which have been observed empirically and guide the design and optimization of future therapeutic ultrasound pulse sequences.

II. EXPERIMENTAL METHODS

A. Experimental apparatus

An overview of the experimental apparatus is provided in Fig. 1 and consists of a dual-HIFU transducer setup for therapeutic ultrasound generation, a multi-element diagnostic array for B-mode imaging and passive acoustic mapping, and a vessel-embedding tissue-mimicking phantom through which pre-formed microbubbles could be made to flow, using a peristaltic pump to control fluid velocity.

Therapeutic ultrasound was generated with two single-element spherical-segment transducers (outer diameter: 64 mm,
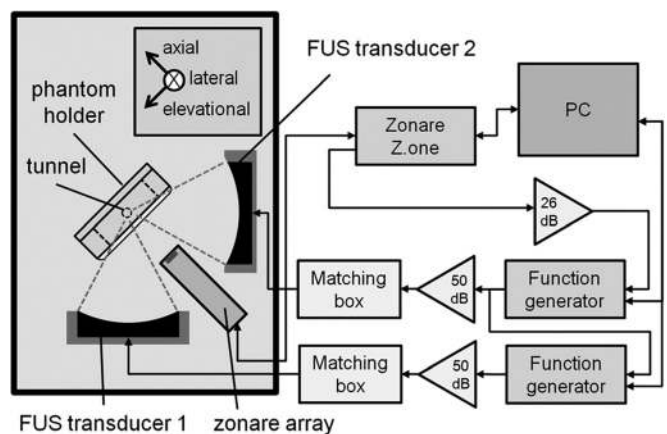

FIG. 1. Overview of experimental apparatus. Two focused ultrasound transducers, the foci of which perpendicularly overlapped, generated therapeutic ultrasound, aimed at a vessel embedded within a tissue mimicking material through which contrast agent suspensions could be made to flow. Each transducer was driven at 500 kHz by a function generator through a 50 dB power amplifier and matching network. A diagnostic linear array (L10-5, Z.one, Zonare), which was placed 36.5 mm from the focal point, was used to acquire B-mode images before sonication and to passively receive acoustic emissions over 64 independent channels during sonication. The Z.one engine was used to digitize and store channel data as well as to trigger the function generators.

radius of curvature: 62.6 mm; Sonic Concepts, Inc., Bothell, WA) the axial lengths of which were perpendicular to each other at a point 65 mm from the transducer surfaces (Fig. 1). Two transducers were utilized to allow for the generation of a smaller focal volume that will be suitable for future *in vivo* small animal experiments and to allow for the diagnostic linear array to be coaxially positioned closer to the tunnel, thereby improving the resolution of the passive acoustic maps. Each transducer was driven at its 0.5 MHz center frequency, which has previously been demonstrated to yield therapeutic effects (Arvanitis *et al.*, 2011; Bazan-Peregrino *et al.*, 2012). The first transducer had a rectangular cutout (dimensions: 45×18 mm^2) and was driven by a function generator (model: 33250 A; Agilent, Santa Clara, CA) through an amplifier (model: A300; Electronics and Innovation, Rochester, NY) and matching network. The second transducer had a circular cutout (inner diameter: 22.6 mm) and was driven by a function generator (model: 33220 A; Agilent) through an amplifier (model: 1140LA; Electronics and Innovation) and matching network. A 75-μm-diameter needle hydrophone (HP Series; Precision Acoustics Ltd., Dorchester, Dorset, Great Britan) was used to align the foci, match the phase, and acquire the beam profile of the two transducers. The combined focused beam had a PRP full width at half-maximum (FWHM) diameter of 5.4 mm $\times$ 1.4 mm $\times$ 3.6 mm along the axial, elevational, and lateral dimensions (Fig. 2). Meanwhile, a 400-μm-diameter hydrophone (model: HNA-0400; Onda Corporation, Sunnyvale, CA) was used to capture pulsed waveforms and calibrate the pressure output generated from the transducers.

The Z.one ultrasound imaging engine (Zonare Medical Systems, Mountain View, CA) with an L10-5 linear array probe (center frequency: 7.14 MHz, bandwidth: 5 MHz) was used for B-mode imaging and passive acoustic mapping. The array was composed of 128 elements with a 38.4-mm aperture, 0.3-mm element spacing, and 5-mm elevational width. In passive acquisition mode, 64 elements of channel data were simultaneously captured and consisted of every other element from the 2nd to 64th and the 65th to 127th.

A 1.6-mm-diameter tunnel phantom (3% agar; Life Technologies, Ltd., Paisley, Great Britain) was manufactured as previously described (Arvanitis *et al.*, 2011) and connected to a closed-loop circuit containing degassed water. The water was pulled from a beaker and through the tunnel using a peristaltic pump (model: Minipuls 2; Gilson, Middleton, WI) and was returned to its origin. The total volume in the tunnel, tubing, and beaker was 295 ml and was calibrated to have mean fluid velocities of 10, 20, or 40 mm/s. Prior to sonication, 5 ml of SonoVue® microbubbles (Bracco Imaging S.p.A., Milan, Italy) or degassed water was added to the beaker to create a total volume of 300 ml and an estimated concentration of 0.3×10^6 to 1.7×10^6 microbubbles per milliliter. To distribute the microbubbles uniformly throughout the circuit, a stir bar continuously mixed the microbubbles in the beaker and the circuit was set at 40 mm/s for 2 min prior to sonication.

The linear array was positioned between the two transducers at a 45° angle and with its lateral length perpendicular to each transducer's axial length (Fig. 1). The focal point of the superimposed beams was placed 36.5 mm from the
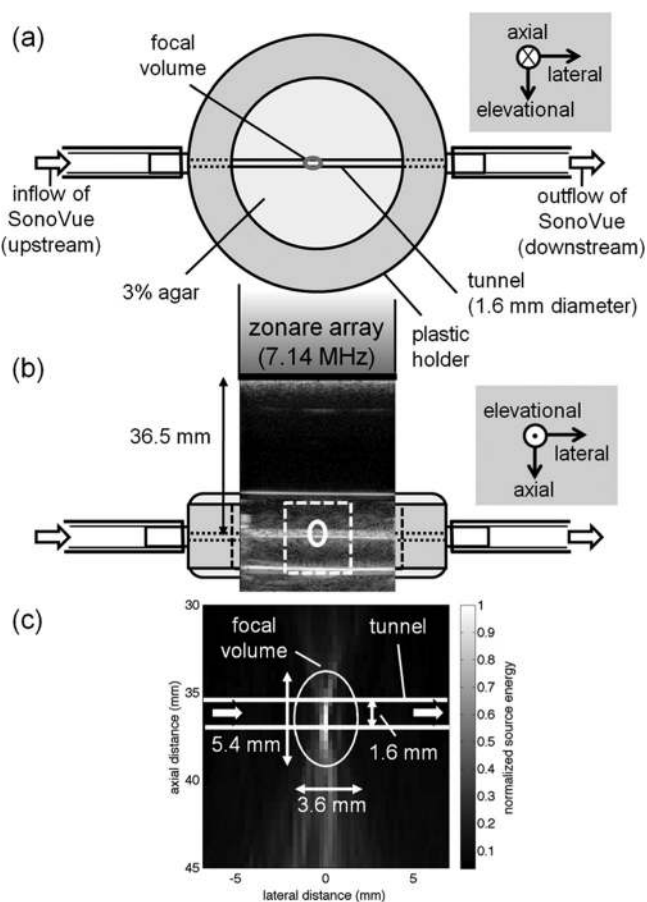

FIG. 2. Tunnel phantom and imaging orientation. (a) A lateral-elevational plane view of the 1.6-mm-diameter tunnel phantom made of 3% agar. The focus of the therapy transducers overlapped with the tunnel, which had SonoVue microbubbles or water only flowing along the lateral axis. (b) Axial-lateral view of the phantom with an overlapping B-mode image. The dotted box in (b) was the region of interest used to generate (c) passive acoustic maps. The axial, lateral, and elevational orientations were relative to the linear array.

probe's surface. The tunnel phantom was placed in the degassed water tank with its tunnel length positioned along the array's lateral axis and overlapping with the focal point (Fig. 2).

B. Experimental design and protocol

The distribution of therapeutic effects of microbubble-perfused tissue exposed to ultrasound has been previously shown to have a spatial bias depending on the exposure conditions (e.g., PRP, PL, and PRF). In this study, spatially biased cavitation activity was investigated both within a pulse, which was expected to depend on the PL and through several pulses, which was expected to depend on the PRF. To perform these analyses, a total of 231 unique sets of experimental conditions were evaluated (Table I). The tunnel phantom was sonicated with a range of ultrasonic parameters [PRP: 100–1500 kPa, PL: 1, 5, 25, 100 000 cycles, pulse repetition frequency (PRF): 1, 5, 10, 50 Hz] at fluid velocities of 10, 20, or 40 mm/s. The reported PRPs were produced by adjusting the transducer's input voltage for each PL to compensate for the transducer's rise time. In addition, the reported PLs

J. J. Choi and C.-C. Coussios: Cavitation dynamics of flowing microbubbles

TABLE I. Ultrasound and tunnel flow parameters.

Experimental set	Peak-rarefactional pressure (kPa)	Pulse length (cycles)	Pulse repetition frequency (Hz)	Number of pulses	Fluid velocity (mm/s)
A	100, 150, 200, 250, 300, 350, 400, 450, 500, 550, 600, 750, 900, 1050, 1200, 1350, 1500	100 000	–	1	40
B	150, 300, 450, 600, 900, 1200, 1500	25	1	10	10, 20, 40
			5	25	
			10	50	
			50	250	
C	100, 150, 200, 250, 300, 350, 400, 450, 500, 550, 600, 750, 900, 1050, 1200, 1350, 1500	1, 5, 25	1	10	10
			50	250	
D (control)	150, 300, 450, 600, 900, 1200, 1500	25	1	10	10
			5	25	
			10	50	
			50	250	

were based on the input waveform, whereas the actual pressure waveform for the shortest PLs were 1.5 and 4.5 cycles.

Analysis of cavitation activity within a pulse was performed using experimental sets A and C listed in Table I. Various PLs were selected including a 100 000-cycle PL, corresponding to 200 ms at a 0.5-MHz center frequency, which was selected because it has been previously shown to be longer than necessary to produce desired bioeffect (Choi *et al.*, 2011a; Choi *et al.*, 2011b; Hynynen *et al.*, 2001; Tung *et al.*, 2010a). Meanwhile, analysis of cavitation activity through several pulses was performed using experimental set B listed in Table I. PRFs of 1, 5, 10, and 50 Hz were selected because they were within a range of parameters typically used in therapeutic applications. Using concepts of destruction-replenishment previously described for the purpose of perfusion imaging (Wei *et al.*, 1998), a critical PRF value PRF_{crit} was calculated by dividing the fluid velocity by the tunnel length where microbubbles were potentially destroyed. Fluid velocities of 10, 20, and 40 mm/s with a destruction length equal to the beam's lateral FWHM of 3.6 mm, corresponded to PRF_{crit} of 2.8, 5.6, and 11.1 Hz, respectively.

C. Passive acoustic mapping

Sixty-four channels of 65-μs-long acoustic emissions were captured as a frame at a sampling frequency of 50 MHz, which was subsequently upsampled to 200 MHz. During sonication with a 100 000-cycle PL, 200 frames of data were passively acquired with the linear array at a 1000-Hz frame rate. During sonications of 1-, 5-, and 25-cycle PLs, a series of 10, 25, 50, and 250 frames were acquired at a 1-, 5-, 10-, or 50-Hz frame rate.

Cavitation activity was characterized by its source strength using a previously described method (Gyöngy and Coussios, 2010a,b). In brief, a bubble centered at $\mathbf{r}$ with a source strength of $q(\mathbf{r},t)$ generates pressure at location $\mathbf{r}'$ and time t given by

$$p(\mathbf{r}', t) = \frac{q(t - |\mathbf{r}' - \mathbf{r}|/c)}{4\pi|\mathbf{r}' - \mathbf{r}|}, \qquad (1)$$

where c is the speed of sound of the medium set to 1480 m s^{-1}. Equation (1) allows an estimate of the source strength $\tilde{q}(\mathbf{r}, t)$, and by extension, the energy $\tilde{E}(\mathbf{r})$ radiated by the bubble

$$\tilde{q}(\mathbf{r}, t) = \frac{1}{N} \sum_{i=1}^{N} 4\pi|\mathbf{r}_i - \mathbf{r}|\tilde{p}(\mathbf{r}_i, t + |\mathbf{r}_i - \mathbf{r}|/c), \qquad (2)$$

$$\tilde{E}(\mathbf{r}) = \int \frac{\tilde{q}^2(\mathbf{r}, t)}{4\pi\rho_0 c} \, dt, \qquad (3)$$

where $\tilde{p}(\mathbf{r}_i, t)$ is the pressure at r_i estimated from the corresponding pressure sensor, and ρ_0 is the (undisturbed) density of the medium set to 1000 kg m^{-3}. Passive maps of source strength and energy were obtained in a 31×57 pixel map with a pixel size of 0.5×0.25 mm [Fig. 2(c)]. Considering the active channels in passive mode, which resulted in a 37.8 mm aperture, the estimated −3 dB lateral and axial resolutions of the maps at the focal point for a 7.14 MHz source was 0.18 and 1.3 mm (Gyöngy and Coussios, 2010b).

D. Data analysis

Decoupling broadband from harmonic and ultraharmonic contributions of the source strength is difficult due to the increasing frequency bandwidth of harmonic components with energy and the fact that harmonic and ultraharmonic components overlap with broadband emissions. Therefore a truly broadband frequency range where no harmonic and ultraharmonic components exist is difficult to claim for the wide range of pressures evaluated in this study. The "harmonic" source strength was obtained by applying a 0.25-MHz-wide band comb filter at integer multiples of the driving ultrasonic frequency ($f_0 = 0.5$ MHz) within the 5–10 MHz bandwidth of the linear array ($10f_0$, $11f_0$, $12f_0$,…, $20f_0$) and spanned a frequency range encompassing potential harmonics and broadband noise. The "nonharmonic" source strength was obtained by applying a similar comb filter offset by 0.25 MHz to capture contributions between integer multiples of the driving frequency and spanned a frequency range encompassing potential ultraharmonics and broadband noise. Harmonic and nonharmonic energy values were then computed using Eq. (3) with their corresponding filtered data. A source strength was
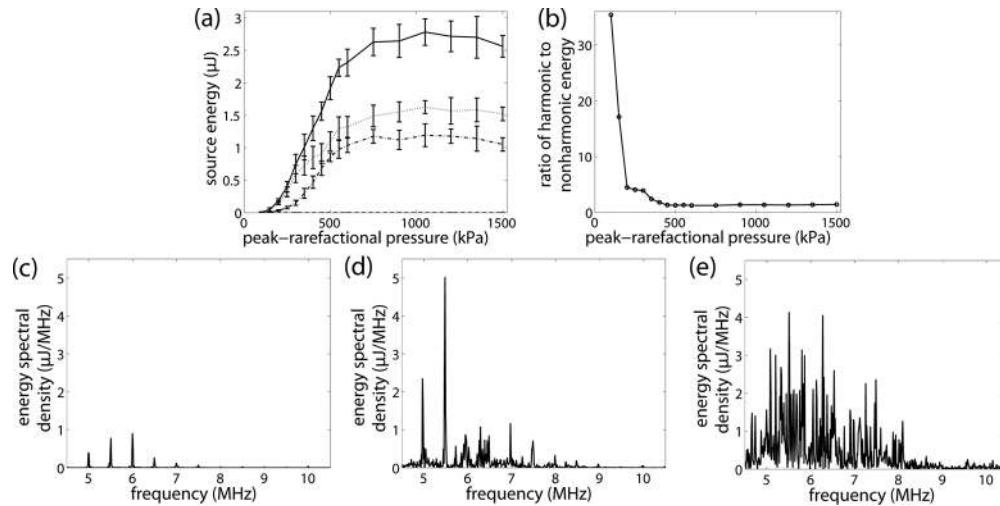
FIG. 3. Type of cavitation activity. SonoVue microbubbles were sonicated at PRPs of 100–1500 kPa with a 25-cycle PL. The fluid velocity was set to 10 mm/s, and the PRF was set to 1 Hz to ensure microbubble replenishment between pulses. (a) The source energy was estimated at the focal point for sonicated (solid line) microbubbles and (dashed line) water only. The energy generated for microbubbles was split into its (dotted line) harmonic and (dashed-dotted line) non-harmonic components. The energy was the mean of 10 pulses while the error bars were standard deviations. (b) The ratio of the harmonic to nonharmonic components dropped rapidly with pressure but stabilized at approximately 1.3 ± 0.3. Frequency-domain plots depict (c) harmonics at 150 kPa, (d) a mixture of harmonic and broadband emissions at 300 kPa, and (e) broadband emissions at 450 kPa.

classified as being harmonic if it had a harmonic to nonharmonic ratio greater than 5, broadband with a ratio less than 1.5, and mixed with ratios between 1.5 and 5. Although ultraharmonics could have contributed to nonharmonic energy values, they were only present in conjunction with harmonics of wider bandwidths and higher amplitudes. Thus the influence of ultraharmonics to the ratio was minimal (Fig. 3).

The distribution of source energy generated was analyzed in two dimensions as PAMs and in one dimension for a single row of pixels along the tunnel. The distribution of cavitation energy in the focal volume was characterized as having or lacking lateral symmetry with the spatial energy ratio, which was calculated by dividing the sum of energy in a 3.5×0.25 mm^2 area immediately upstream of the focal point by the sum of energy in a 3.5×0.25 mm^2 area downstream of the focal point.

In many of the measurements, high levels of broadband energy were recorded in the first few milliseconds of a pulse or a series of pulses. The duration of this initial broadband activity was arbitrarily defined as the time point where broadband energy reached 25% of its initial magnitude.

III. RESULTS

A. Cavitation threshold of SonoVue® microbubbles

The extent a microbubble exposed to ultrasound will be modulated or destroyed will depend on the type, magnitude, and duration of cavitation activity it undergoes. The first investigation of the larger study was therefore to determine the PRP at which a microbubble will transition from stable to inertial cavitation. The source energy generated at the focal point with and without microbubbles was estimated for PRPs of 100–1500 kPa [Fig. 3(a)]. A PL of 25 cycles was selected because increasing the length further would not likely influence the cavitation threshold (Church, 2005). Ten pulses were emitted at a 1-Hz PRF, which ensured complete replenishment between pulses given the set 10-mm/s fluid velocity.

Without microbubbles, the magnitude of energy generated for all PRPs evaluated was significantly less than with microbubbles (P value < 0.05) and was essentially at the noise level of the probe. With microbubbles, the mean source energy rose rapidly until approximately 500 kPa where it then slowed and eventually plateaued. At the lowest two PRPs evaluated (100 and 150 kPa), harmonics of the driving frequency contributed greater than a factor of 5 over the nonharmonic frequency ranges [Fig. 3(b)], which appeared as strong harmonic peaks within the bandwidth of the linear array [Fig. 3(c)]. Further escalating the pressure resulted in emissions energy from both the harmonic and nonharmonic ranges [Fig. 3(d)]. At 450 kPa and above, the ratio of harmonic to nonharmonic energy stabilized at approximately 1.3 ± 0.1, which was due to broadband spectral energy [Figs. 3(b) and 3(e)]. In subsequent analyses, PRPs of 150, 300, 450, and 900 kPa are used as examples of stable, mixed, inertial, and high magnitude inertial cavitation regimes.

B. Cavitation dynamics within a single pulse

As of yet, determining cavitation dynamics within a pulse has been difficult due to the inability to spatially and temporally resolve sources of cavitation activity. Microbubble-seeded cavitation dynamics were analyzed for a range of short (1, 5, and 25 cycles) and long (100 000 cycles) PLs. For the short PLs, the fluid velocity was set to 10 mm/s, and the mean and standard deviations of the source energy was calculated across 10 pulses emitted at a PRF of 1 Hz. In the one-cycle PL case, the source energy steadily increased throughout the full range of PRPs evaluated (100–1500 kPa) [Fig. 4(a)]. A similar rise was observed for 5- and 25-cycle PLs until approximately 500 kPa, where the rate of energy rise began to decrease. For the short PLs evaluated, the energy of acoustic emissions generated were laterally symmetric as indicated by spatial energy ratios of 1.1 ± 0.3, 1.1 ± 0.2, and 1.0 ± 0.1 across all PRPs for

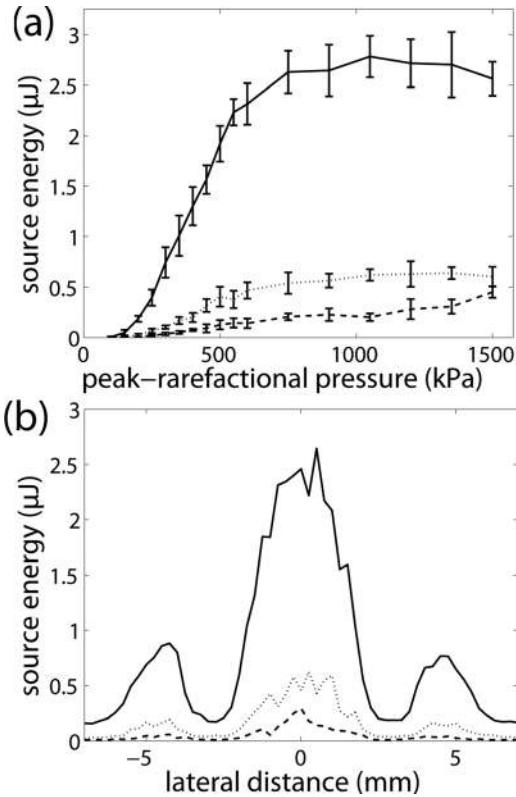J. J. Choi and C.-C. Coussios: Cavitation dynamics of flowing microbubbles

FIG. 4. Magnitude and spatial distribution of cavitation activity within short-PL pulses. SonoVue microbubbles were sonicated at PRPs of 100–1500 kPa. The fluid velocity was set to 10 mm/s and the PRF was set to 1 Hz. (a) The total energy of acoustic emissions was measured for PLs of (dashed line) 1, (dotted line) 5, and (solid line) 25 cycles. The plotted energy was the mean of 10 pulses while the error bars indicate standard deviations. (b) The spatial distribution of cavitation energy for a single pulse was laterally symmetric at a PRP of 900 kPa for PLs of (dashed line) 1, (dotted line) 5, and (solid line) 25 cycles.

PLs of 1, 5, and 25 cycles, respectively. At 900 kPa, good lateral symmetry is qualitatively observed for the three PLs [Fig. 4(b)].

In the long PL case, acoustic emissions were monitored for a single 100 000-cycle (200 ms) PL with a 40 mm/s fluid velocity. In general, the total source energy increased rapidly at low PRPs until it reached a maximum at 300 kPa [Fig. 5(a)]. Beyond this PRP, the total energy decreased and then stabilized. The initial rise in energy between 100 and 300 kPa was due to a steady rise in cumulative energy throughout the entire length of the pulse [Fig. 5(b)]. Qualitatively, the spatial distribution of energy at 150 kPa had a similar distribution as the FUS beam profile [Fig. 5(c)]. However, careful analysis of the distribution shows a sub-millimeter shift upstream as indicated by a spatial energy ratio of 1.4. Analysis of time portions of the spatial energy ratio indicates a spatial energy ratio of approximately 1 in the first few milliseconds of the pulse followed by a gradual increase until approximately 50 ms where it then stabilizes near 1.5 [Fig. 5(d)]. The source energy at 150 kPa was mainly due to harmonics and subharmonics [Fig. 6(a)]. At 300 kPa where the maximum source energy was generated, a steep rise in cumulative energy was followed by a steady rise throughout the rest of the pulse [Fig. 5(b)]. Qualitatively, the distribution was not laterally symmetric [Fig. 5(c)] due to a rapid rise in the spatial energy ratio in the first few milliseconds, followed by a steady rise to 2.3 [Fig. 5(d)]. Spectral analysis reveals large magnitudes of broadband energy in the first 7 ms of the pulse followed by a large and steady level of harmonics thereafter [Fig. 6(b)]. The initial broadband energy duration had good correlation with the steep rise in cumulative energy and spatial energy ratio. At 450 kPa, the source energy initially rose at a higher rate than that of 300 kPa but was followed by a lower rate of energy
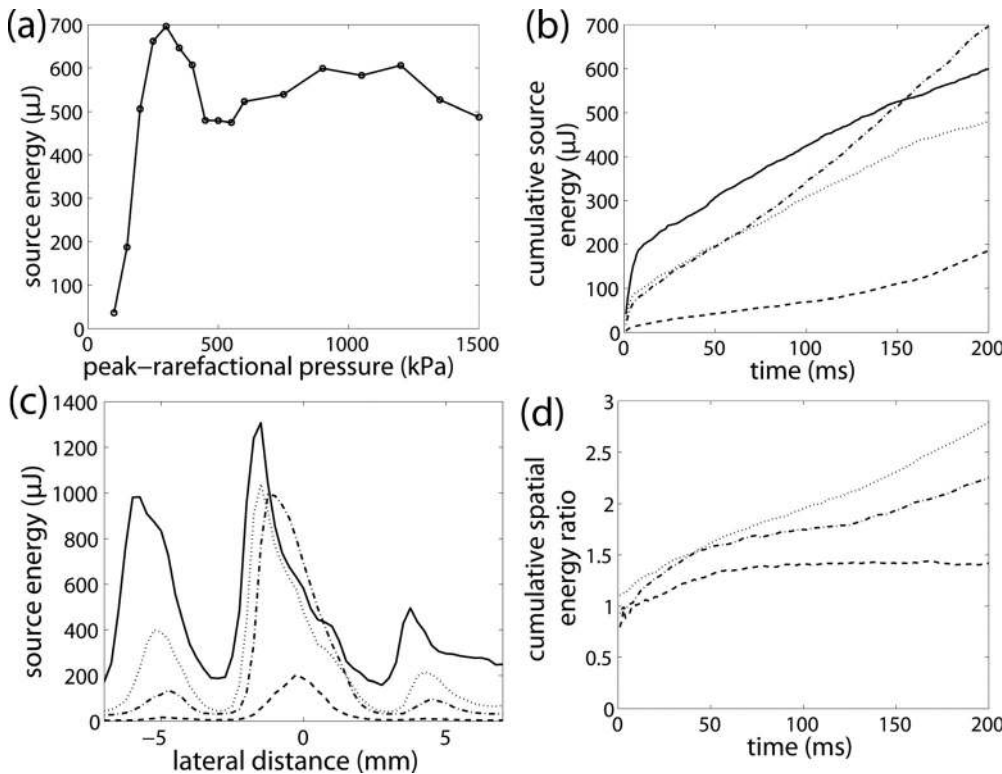

FIG. 5. Magnitude and spatial distribution of cavitation activity within a long-PL pulse. SonoVue microbubbles were sonicated at PRPs of 100–1500 kPa, and the fluid velocity was set to 40 mm/s. (a) The source energy was estimated across the full 100 000-cycle-PL, which corresponded to 200 ms. (b) The cumulative source energy depicts the time portion at which the energy accumulated during the pulse, (c) the spatial distribution of energy depicts the existence or lack of lateral symmetry, and (d) the cumulative spatial energy ratio depicts the time portion at which these biases were accumulated. The plots in (c) amd (d) show results for PRPs of (dashed line) 150, (dashed-dotted line) 300, (dotted line) 450, and (solid line) 900 kPa.
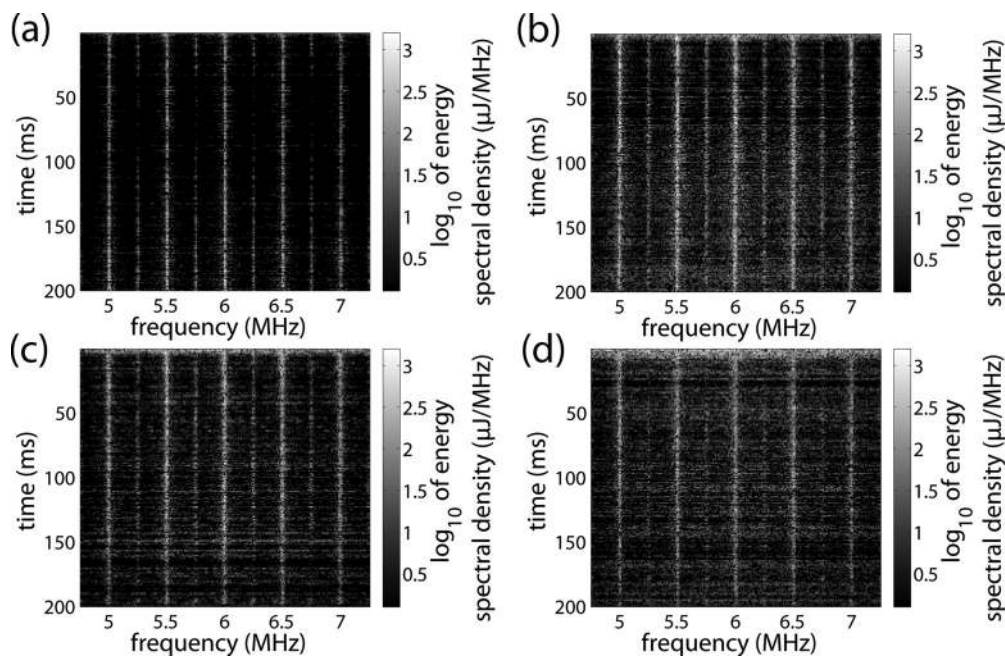
FIG. 6. Spectrum of cavitation activity within a long-PL pulse. SonoVue microbubbles were sonicated with a 100 000-cycle PL with a fluid velocity of 40 mm/s. Sonications were applied at PRPs of (a) 150, (b) 300, (c) 450, and (d) 900 kPa.

emissions [Fig. 5(b)]. After the full 200 ms, the focal point's total source energy at 450 kPa was actually lower than at 300 kPa. The distribution of this energy was not laterally symmetric with a spatial energy ratio of 2.9 [Fig. 5(c)] and was composed of a large level of broadband energy initially followed by a mixture of harmonic and broadband energy thereafter [Fig. 6(c)]. At 900 kPa, the energy generated rose rapidly at the beginning of the PL but then the rate of increase dropped soon after [Fig. 5(b)]. The distribution of this energy was even further spatially biased upstream as can be observed with the large difference in the side lobes [Fig. 5(c)]. The sharp initial rise and spatial bias correlate wells with large levels of broadband events in the first 6 ms [Fig. 6(d)]. At PRPs in the inertial cavitation regime, the largest magnitude of broadband energy was observed in the first 6.3 ± 1.3 ms.

The type and magnitude of cavitation activity within a pulse changed with both space and time. As an example, sonication at 450 kPa, which was in the inertial cavitation regime, produced strikingly different magnitudes and spatial distributions of cavitation activity between the first and last pulse [Figs. 7(a) and 7(b)]. Not only did the maximum cavitation energy decrease, but also, the energy at the focal point and downstream portion of the FUS beam was significantly lower than the upstream portion. The cumulative map reveals a spatial bias upstream and a depletion of energy downstream [Fig. 7(c)]. At the focal point, large broadband acoustic emissions are detected in the first few milliseconds of the pulse followed by harmonics that decreased in amplitude with time [Fig. 7(f)]. Meanwhile, comparison of the source energy of the upstream and downstream portions of
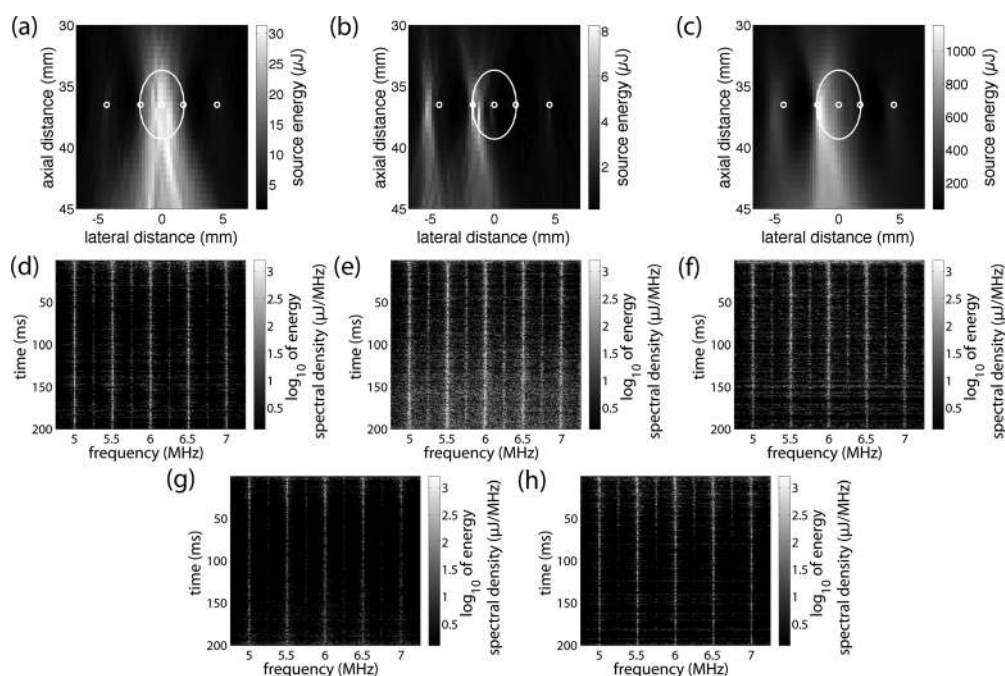

FIG. 7. Cavitation dynamics within a long-PL pulse. SonoVue microbubbles were sonicated at 450 kPa with a 100 000-cycle PL with a fluid velocity of 40 mm/s. Passive acoustic maps of the (a) start, (b) end, and (c) accumulation of the entire pulse depict changes in the magnitude and spatial distribution of cavitation activity. The white circles in (a)—(c) from left to to right represent five spatial locations of cavitation activity the spectrums of which are plotted in (d)—(h). The large white ellipse in (a)—(c) represents the location and FWHM dimension of the FUS beam.
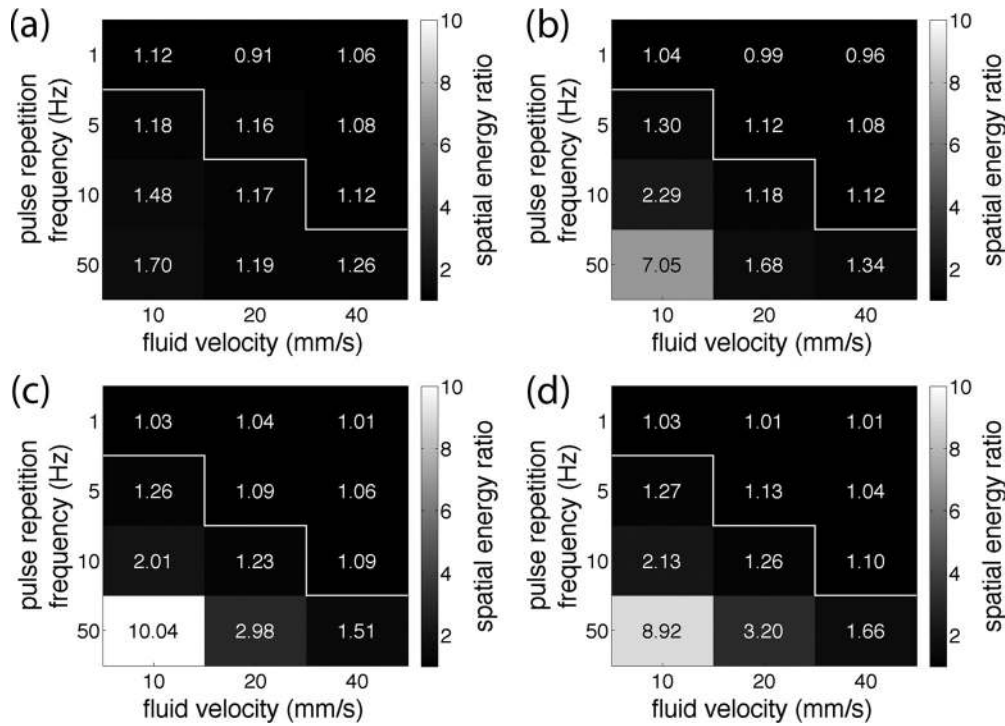
FIG. 8. Spatial distribution of cavitation activity through several pulses. SonoVue microbubbles flowing at fluid velocities of 10, 20, and 40 mm/s were sonicated at PRFs of 1, 5, 10, and 50 Hz for 5 s. The spatial energy ratios were measured at PRPs of (a) 150, (b) 300, (c) 450, and (d) 900 kPa. The spatial energy ratio calculated at 900 kPa is not representative of the true distribution because significant cavitation activity was present in the side lobes. The white line was placed between the PRFs where the PRF_{crit} would be.

the main lobe's FWHM depicts different amplitudes. The upstream portion depicts steady harmonics throughout the entire PL followed by increasingly large magnitudes of broadband events [Fig. 7(e)]. The downstream pixel depicted harmonics that decreased with time [Fig. 7(g)].

C. Cavitation dynamics through several pulses

Following exposure to a pulse of ultrasound, a time interval without any exposure is typically required to allow for intact and undisturbed microbubbles to replenish the focal volume. The optimal interval time, and therefore the PRF, at which microbubbles are exposed to is therefore dependent on the flow rate within the vasculature. In this study, the evolution of microbubble-seeded cavitation dynamics through several pulses was evaluated at a 25-cycle PL for a range of PRPs (150–1500 kPa), PRFs (1, 5, 10, and 50 Hz), and flow conditions (10, 20, and 40 mm/s). For all PRPs at PRFs below PRF_{crit}, the energy generated increased linearly with the number of pulses emitted, the type of cavitation generated was the same throughout all the pulses, the cavitation energy was spatially distributed according to the shape of the beam profile, and the spatial energy ratio was approximately 1 (Figs. 8 and 9).
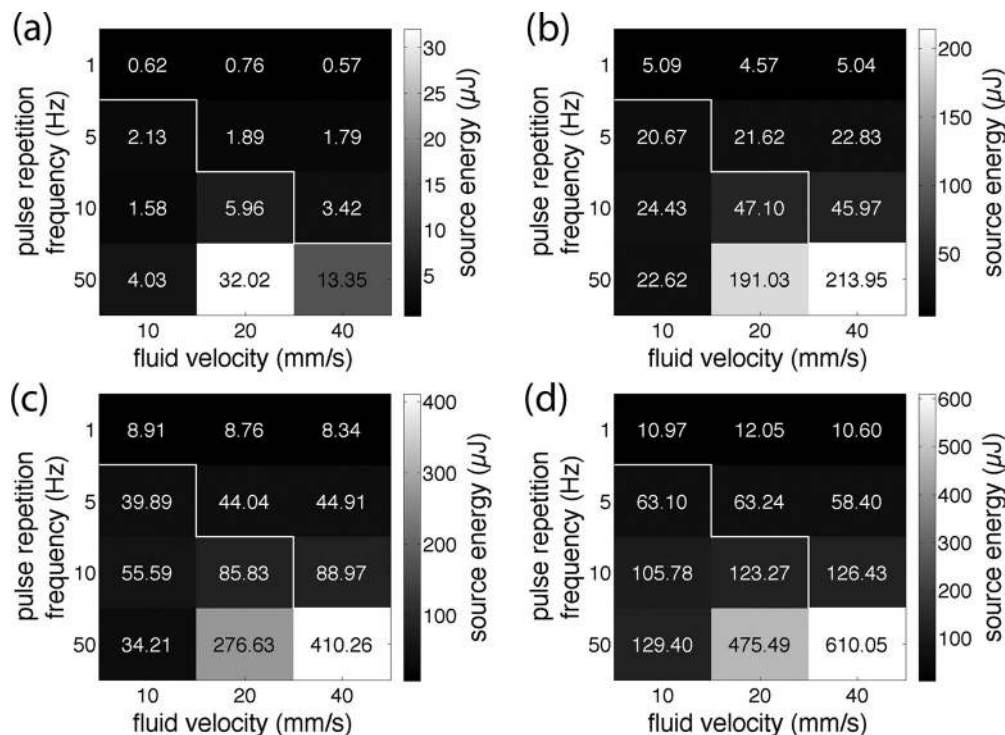

FIG. 9. Magnitude of cavitation activity through several pulses. SonoVue microbubbles flowing at fluid velocities of 10, 20, and 40 mm/s were sonicated at PRFs of 1, 5, 10, and 50 Hz for 5 s. The source energy was estimated at PRPs of (a) 150, (b) 300, (c) 450, and (d) 900 kPa. The white line was placed between the PRFs where the PRF_{crit} would be.

At PRFs above PRF$_{crit}$, the evolution of cavitation dynamics was dependent on the cavitation regime. At 150 kPa, the highest spatial energy ratio of 1.7 was generated with a 50-Hz PRF and a 10-mm/s fluid velocity [Fig. 8(a)], while the highest energy was produced with a 50-Hz PRF and a 20-mm/s fluid velocity [Fig. 9(a)]. The source energy at 150 kPa was mostly from harmonics maintained throughout all 250 pulses [Fig. 10(a)]. At PRPs of 300 kPa and greater, the spatial energy ratio rose with increasing PRF and decreasing fluid velocities (Fig. 8) so that a 50-Hz PRF and 10-mm/s fluid velocity consistently produced the highest spatial energy ratio. The highest source energy at a given PRP was at the highest PRF and flow rate of 50 Hz and 40 mm/s, respectively. Also, if both the PRP and PRF are set constant, increasing fluid velocities produced higher source energy. However, increasing the PRF given a constant PRP and fluid velocity did not necessarily produce greater energy. With a 10-mm/s fluid velocity and 300- and 450-kPa PRPs, the greatest energy generated at the focal point was at a 10-Hz PRF. In other words, a 10-Hz PRF at the 10-mm/s fluid velocity produced a greater focal point source energy than at 50 Hz, the latter which had five times more pulses emitted. At these PRPs, broadband emissions dominated the first few pulses at 50 Hz, which was then followed by lower magnitudes of broadband energy mixed with harmonics and ultraharmonics. At 900 kPa, the highest source energy with a 10-mm/s fluid velocity was at a 50-Hz PRF. However, the energy rise from a PRF of 1–50 Hz was not linear [Fig. 9(d)]. Broadband emissions were present through almost every pulse emitted [Fig. 10(d)].

Cavitation dynamics through several pulses changed with both space and time. As an example, sonication with a 450-kPa PRP and 25-cycle PL pulse emitted at a 50-Hz PRF produced strikingly different magnitudes and spatial distributions of cavitation activity between the first and last pulse [Figs. 11(a) and 11(b)]. Not only did the source energy at the focal point decrease over time, but also the downstream portion of the FUS beam decreased when compared to the upstream portion. The cumulative map also depicts a spatial bias upstream [Fig. 11(c)]. At the focal point, broadband sources are detected in the first few pulses followed by harmonics and the recurrence of lower magnitudes of broadband emissions throughout the rest of the sonication [Fig. 11(f)]. The upstream and downstream portions of the main lobe's FWHM depict drastically different magnitudes. The upstream portion depicts strong harmonic and broadband energy throughout all the pulses [Fig. 11(e)]. Meanwhile, the downstream portion depicts harmonic and broadband energy in the first few pulses, which are nearly depleted in energy thereafter [Fig. 11(g)].

IV. DISCUSSION

A. Cavitation dynamics within a pulse

The fundamental unit of therapeutic ultrasound is the pulse, which, for the purpose of cavitation, is often described by its center frequency, PRP, and PL. A microbubble exposed to a pulse can expand and contract to the driving frequency's rarefactional and compressional phases, respectively. Previous work has shown that at low PRPs, stable cavitation can be maintained for several acoustic cycles where rectified diffusion, shrinkage, or radiation forces increasingly occur (Apfel, 1997). Our results at 100 000 cycles and a 150-kPa PRP produced stable cavitation as indicated by the absence of broadband emissions [Fig. 6(a)] and the generation of a steady magnitude of source energy throughout the entire length of the pulse [Fig. 5(b)]. However, the spatial energy ratio was 1.5 [Fig. 5(d)], which appeared qualitatively as a sub-millimeter spatial shift upstream [Fig. 5(c)]. Although the cause of the spatial shift is uncertain, it may be due to radiation force pushing bubbles away from the focal point.

At PRPs above the inertial cavitation threshold, microbubbles can expand to several times their equilibrium radius and subsequently collapse due to the inertia of the surrounding media, an event that produces broadband emissions. This
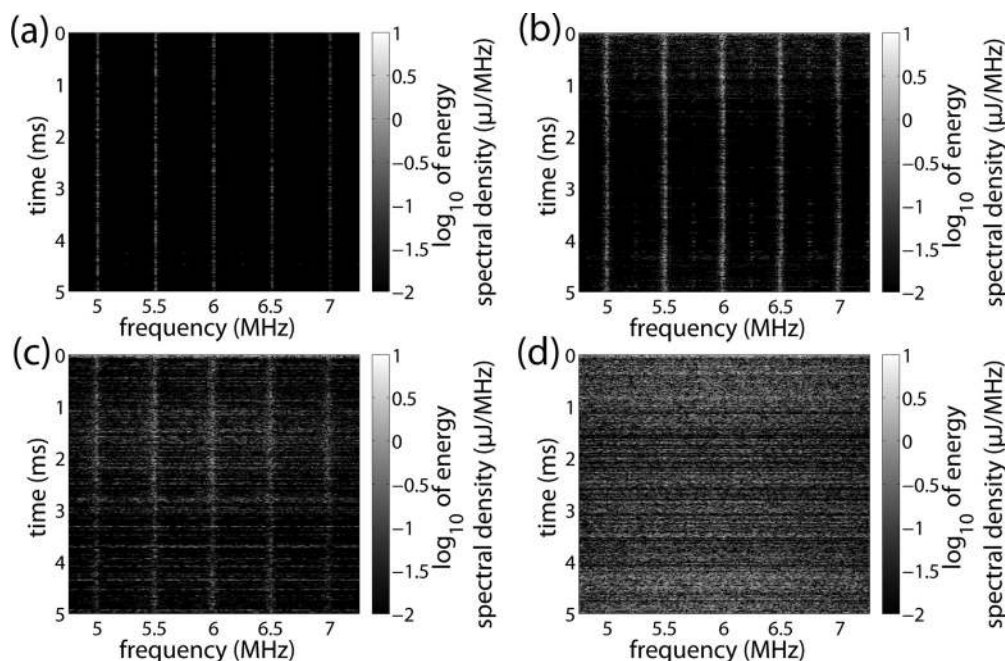

FIG. 10. Spectrum of cavitation activity through several pulses. SonoVue microbubbles flowing at a fluid velocity of 10 mm/s was sonicated with a 25-cycle PL at a PRF of 50 Hz for 5 s. Sonications were applied at PRPs of (a) 150, (b) 300, (c) 450, and (d) 900 kPa.
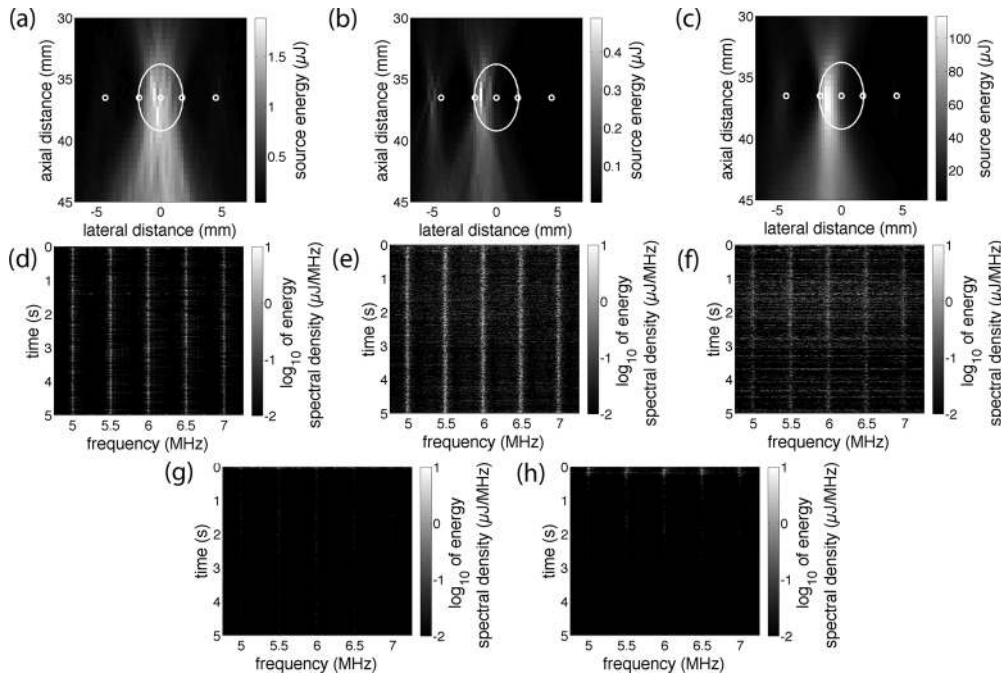
FIG. 11. Cavitation dynamics through several pulses. SonoVue microbubbles were sonicated at 450 kPa with a 25-cycle PL, 50-Hz PRF, and 10-mm/s fluid velocity. Passive acoustic maps of the (a) first, (b) last, and (c) accumulation of all pulses depict changes in the magnitude and spatial distribution of cavitation activity. The white circles in (a)—(c) from left to to right represent five spatial locations of cavitation activity the spectrums of which are plotted in (d)—(h). The large white ellipse in (a)—(c) represents the location and FWHM dimension of the FUS beam.

collapse can occur over several cycles, but, as observed in our studies, was limited to the first 6.3 ± 1.3 ms of the pulse regardless of the applied PRP [Figs. 6(c) and 6(d)]. The high magnitude broadband source in the first few milliseconds of the pulse was the cause for the large initial rise in source energy [Fig. 5(b)]. Two different trends were subsequently produced. At PRPs with mixed spectral content, the large broadband emissions were followed by a steady rise of energy throughout the rest of the pulse that were dominated by its harmonic component. At PRPs well above the inertial cavitation threshold, the initial broadband energy generated was larger but was followed by a slower rise of energy thereafter. This disparity may originate from the polydispersed size distribution of microbubbles, and, because the cavitation threshold is size-dependent, bubbles at different sizes may have experienced inertial cavitation while others may have persisted throughout the entire pulse (Samuel et al., 2009b). The latter effect is suggested by the large harmonics generated throughout the length of the pulse. At PRPs well above the inertial cavitation threshold, very high levels of broadband energy were generated, but, because a larger population of microbubbles was destroyed, further generation of energy was dependent on the inflow of new cavitation nuclei. The result was lower source energy at the focal point than at PRPs near the threshold and spatially biased distributions [Figs. 5(c) and 5(d)].

B. Cavitation dynamics through several pulses

Microbubbles can be destroyed during sonication through diffusion and dissolution of the encapsulated gas and/or fragmentation of the bubble shell. Because most therapeutic ultrasound applications utilize multiple pulses with parameters within the destruction regime, a time interval void of ultrasound is required to allow for replenishment of cavitation nuclei throughout the focal volume. Destruction-replenishment kinetics has been most widely studied for perfusion imaging where a high PRP destruction pulse is followed by low PRP imaging pulses to track the microbubbles

as they continue to replenish the vasculature (Wei et al., 1998). In these studies, the rate of microbubble replenishment was shown to be a function of the flow rate and beamwidth (Hudson et al., 2009; Hudson et al., 2011). Meanwhile, similar concepts of replenishment have been extended to therapeutic ultrasound as it is becoming increasingly apparent that it affects the dose, distribution, and efficiency of drug delivery or therapeutic action (Choi et al., 2011a; Choi et al., 2011b; Goertz et al., 2010). Because the vascular environment of the tissue typically cannot be modulated, the main method for controlling therapeutic outcome is through selection of the PRF.

In the present study, the effects of fluid velocity and PRF on cavitation activity followed a few general trends. Sonication at PRFs below PRF_{crit} produced predictable cavitation dynamics regardless of PRP due to complete replenishment of the focal volume. However, these trends did not hold with sonications at PRFs above the PRF_{crit} as cavitation dynamics could change markedly from pulse to pulse. The greatest spatial bias in cavitation activity distribution was greatest at PRFs furthest from the PRF_{crit} and was most likely due to microbubble destruction and subsequent entry of new nuclei upstream, which were subsequently destroyed before they could reach the downstream portion. The maximum energy at a given PRF was at the largest fluid velocity. Meanwhile, given a fluid velocity, increasing the PRF did not necessarily increase the maximum energy generated. This latter effect is also likely due to a balance between sufficient number of emitted pulses and sufficient number of nuclei present.

The type and magnitude of cavitation activity generated in the first few milliseconds of a long PL pulse or the first few pulses was predictable and consistent. However, as the PL increased or as a greater number of pulses were emitted at a high PRF, changes to the type and magnitude of cavitation activity were observed. As with long PLs, a large percentage of total source energy generated at high PRFs was from the first few milliseconds. However, in contrast to long PLs, several pulses produced less steady levels of harmonics and broadband

noise. For example, there was an increased presence of broad-band emissions in subsequent pulses when several pulses were emitted [Figs. 10(c) and 10(d)]. Another observed difference was the stark contrast in harmonics generated in the left side lobe and left FWHM portion of the main lobe compared to the contralateral points where, after the few pulses, there was nearly a complete depletion of harmonic energy. The time between pulses (20 ms) may have allowed for a greater time period where gas could diffuse into the surrounding water to allow for complete destruction of most of the bubbles and where new microbubbles could refill at least portions of the focal volume.

C. Limitations and clinical relevance

Microbubble-mediated acoustic cavitation dynamics were monitored in a 1.6-mm diameter tunnel phantom, which was composed of 3% agar. This experimental setup was designed to model destruction-replenishment kinetics and was similar to what has been used previously (Hudson et al., 2009; Wei et al., 1998). However, the in vivo vasculature is composed of arteries, veins, and capillaries, which have different diameters, vessel stiffness, angle, and flow rates, which our model does not account for. Several studies have shown that cavitation dynamics depend on vascular characteristics (Qin and Ferrara, 2006, 2010; Sassaroli and Hynynen, 2007), and our model should be carefully considered in light of this. Particularly important is vessel size, which can affect the oscillating microbubble's boundary conditions and, in capillaries, can constrain the maximum size of bubble expansion (Caskey et al., 2007; Chen et al., 2011). A sonication target of a heterogeneous vasculature could then be expected to have a wide range of types and magnitudes of cavitation activity occurring in the focal volume. The cavitation threshold in such a system could differ from the threshold measurements obtained in the present study by having a wider PRP range where both harmonic and broadband components were present. Regardless, many of the observed relationships among the cavitation dynamics and ultrasonic parameters in our study should hold and the in vivo vasculature should differ from our phantom model mainly in the time scale and distribution of events but not the order of events.

D. Pulse sequence design for therapeutic ultrasound

Effective and safe ultrasound-mediated ultrasound therapy entails careful consideration of the full spatiotemporal dynamics of cavitation activity. The effects of any single ultrasonic parameter cannot be viewed independently of the rest of the characteristics of the pulse sequence design especially because the tissue contains flowing cavitation nuclei throughout a heterogeneous vasculature. As demonstrated in this paper, the effects of flow influence not only pulse to pulse replenishment phenomena, but also heavily influence the spatial distribution of cavitation activity within a pulse. One of the aims of ultrasound-enhanced drug delivery is to enhance not only the dose but also the distribution of molecular agents throughout the sonicated region. Several studies evaluating blood-brain barrier disruption have shown that long PLs of 20 ms produce a more heterogeneous distribution of drug delivery than shorter 50-cycle PLs (Choi et al., 2010; Choi et al., 2011a; Choi et al., 2011b). In the present study, increasing the PL resulted in a higher spatial bias

upstream and reduced the efficiency of generating cavitation activity at the focal point and downstream portions of the main and side lobes. Therefore a possible mechanism for the heterogeneous distribution of drugs in blood-brain barrier disruption is that with long PLs of 20 ms, cavitation activity is initially generated throughout the entire focal volume, which includes all levels of the vasculature. As microbubbles are destroyed, incoming microbubbles are the remaining sites of cavitation activity, thus overexposing large upstream vessels such as arteries and underexposing capillaries, which are the target sites of drug transfer. In one of the previous studies, large punctate regions of fluorescence were present in the larger vascular branches when using long 20-ms PL pulses (Choi et al., 2010; Choi et al., 2011a; Choi et al., 2011b).

Several studies have previously demonstrated that the PRF effects the efficiency of generating cavitation energy (Goertz et al., 2010; Samuel et al., 2009a). The results of the present work confirm these studies as PRFs greater than PRF_{crit} did not result in a linear increase with the number of pulses emitted (Fig. 9). If the goal was to generate the maximum energy at the focus, there appeared to be a balance between microbubble replenishment and emitting a sufficient number of pulses. However, in addition to measuring the magnitude of energy, the present study evaluates the spatial distribution of energy. PRFs furthest from the PRF_{crit} produced the highest spatial bias upstream, thus indicating off-focal point microbubble destruction without proper replenishment. Cavitation dynamics evolved in drastically different directions with the upstream portion of energy being greater than a 10-fold increase over the downstream portion of the FUS beam.

E. Conclusion

The purpose of this paper was to understand how microbubble-seeded cavitation dynamics spatially and temporally evolved during ultrasonic exposure in a flow environment. In this endeavor, passive acoustic mapping was essential due to its ability to resolve key transitions in cavitation activity in both space and time. In particular, the effects of peak-rarefactional pressure, pulse length, and pulse repetition frequency on the type, magnitude, distribution, and duration of cavitation activity were determined. At low peak-rarefactional pressures, stable cavitation was maintained both within a pulse and through several pulses regardless of the length of the pulse or the number of pulses emitted. This resulted in a linear increase of cavitation energy with time and a cavitation distribution within the focal volume that had a low upstream spatial bias. At high peak-rarefactional pressures, inertial cavitation was generated in the first 6.3 ± 1.3 ms of the pulse, where it then remained below 25% of its initial magnitude and increasingly generated a high upstream spatial bias. When considering several pulses, sonication at pulse repetition frequencies below a critical rate produced no spatial bias and generated energy in a linear manner with time. However, above the critical rate, the energy generated became more unpredictable and upstream spatial bias increased with lower flow rates and higher pulse repetition frequencies. In conclusion, the selection of key ultrasonic parameters in conjunction with an understanding of microbubble destruction and vessel fluid velocities were shown to be critical

in producing a specific type, magnitude, distribution, and duration of cavitation activity within the main focal volume. Passive acoustic mapping with a diagnostic linear array was critical in our mechanistic understanding of these phenomena, and future work entails implementing the methods developed in this study to monitor therapy *in vivo*.

ACKNOWLEDGMENTS

Apfel, R. E. (**1997**). "Sonic effervescence: A tutorial on acoustic cavitation," J. Acoust. Soc. Am. **101**, 1227–1237.

Arvanitis, C. D., Bazan-Peregrino, M., Rifai, B., Seymour, L. W., and Coussios, C.-C. (**2011**). "Cavitation-enhanced extravasation for drug delivery," Ultrasound Med. Biol. **37**, 922–934.

Baseri, B., Choi, J. J., Tung, Y.-S., and Konofagou, E. E. (**2010**). "Multi-modality safety assessment of blood-brain barrier opening using focused ultrasound and definity microbubbles: A short-term study," Ultrasound Med. Biol. **36**, 1445–1459.

Bazan-Peregrino, M., Arvanitis, C. D., Rifai, B., Seymour, L. W., and Coussios, C.-C. (**2012**). "Ultrasound-induced cavitation enhances the delivery and therapeutic efficacy of an oncolytic virus in an in vitro model," J. Controlled Release **157**, 235–242.

Bekeredjian, R., Grayburn, P. A., and Shohet, R. V. (**2005**). "Use of ultrasound contrast agents for gene or drug delivery in cardiovascular medicine," J. Am. Coll. Cardiol. **45**, 329–335.

Caskey, C. F., Stieger, S. M., Qin, S., Dayton, P. A., and Ferrara, K. W. (**2007**). "Direct observations of ultrasound microbubble contrast agent interaction with the microvessel wall," J. Acoust. Soc. Am. **122**, 1191–1200.

Chen, H., Kreider, W., Brayman, A. A., Bailey, M. R., and Matula, T. J. (**2011**). "Blood vessel deformations on microsecond time scales by ultrasonic cavitation," Phys. Rev. Lett. **106**, 034301.

Choi, J. J., Pernot, M., Small, S. A., and Konofagou, E. E. (**2007**). "Noninvasive, transcranial and localized opening of the blood-brain barrier using focused ultrasound in mice," Ultrasound Med. Biol. **33**, 95–104.

Choi, J. J., Selert, K., Gao, Z., Samiotaki, G., Baseri, B., and Konofagou, E. E. (**2011a**). "Noninvasive and localized blood-brain barrier disruption using focused ultrasound can be achieved at short pulse lengths and low pulse repetition frequencies," J. Cereb. Blood Flow Metab. **31**, 725–737.

Choi, J. J., Selert, K., Vlachos, F., Wong, A., and Konofagou, E. E. (**2011b**). "Noninvasive and localized neuronal delivery using short ultrasonic pulses and microbubbles," Proc. Natl. Acad. Sci. U.S.A. **108**, 16539–16544.

Choi, J. J., Wang, S., Tung, Y.-S., Morrison, B., and Konofagou, E. E. (**2010**). "Molecules of various pharmacologically-relevant sizes can cross the ultrasound-induced blood-brain barrier opening in vivo," Ultrasound Med. Biol. **36**, 58–67.

Chomas, J. E., Dayton, P., May, D., and Ferrara, K. (**2001**). "Threshold of fragmentation for ultrasonic contrast agents," J. Biomed. Opt. **6**, 141–150.

Church, C. (**2005**). "Frequency, pulse length, and the mechanical index," ARLO **6**, 162–168.

Coussios, C.-C., and Roy, R. A. (**2008**). "Applications of acoustics and cavitation to noninvasive therapy and drug delivery," Annu. Rev. Fluid Mech. **40**, 395–420.

Daffertshofer, M., Gass, A., Ringleb, P., Sitzer, M., Sliwka, U., Els, T., Sedlaczek, O., Koroshetz, W. J., and Hennerici, M. G. (**2005**). "Transcranial low-frequency ultrasound-mediated thrombolysis in brain ischemia: Increased risk of hemorrhage with combined ultrasound and tissue plasminogen activator: Results of a phase II clinical trial," Stroke **36**, 1441–1446.

Datta, S., Coussios, C.-C., Ammi, A. Y., Mast, T. D., de Courten-Myers, G. M., and Holland, C. K. (**2008**). "Ultrasound-enhanced thrombolysis using Definity as a cavitation nucleation agent," Ultrasound Med. Biol. **34**, 1421–1433.

Datta, S., Coussios, C.-C., McAdory, L. E., Tan, J., Porter, T., De Courten-Myers, G., and Holland, C. K. (**2006**). "Correlation of cavitation with ultrasound enhancement of thrombolysis," Ultrasound Med. Biol. **32**, 1257–1267.

Deng, C., Sieling, F., and Pan, H. (**2004**). "Ultrasound-induced cell membrane porosity," Ultrasound Med. Biol. **30**, 519–526.

Ferrara, K., Pollard, R., and Borden, M. (**2007**). "Ultrasound microbubble contrast agents: Fundamentals and application to gene and drug delivery," Annu. Rev. Biomed. Eng. **9**, 415–447.

Fischer, K., McDannold, N. J., Zhang, Y., Kardos, M., Szabo, A., Szabo, A., Reusz, G. S., and Jolesz, F. A. (**2009**). "Renal ultrafiltration changes induced by focused US," Radiology **253**, 697–705.

Goertz, D. E., Wright, C., and Hynynen, K. (**2010**). "Contrast agent kinetics in the rabbit brain during exposure to therapeutic ultrasound," Ultrasound Med. Biol. **36**, 916–924.

Gyöngy, M., and Coussios, C.-C. (**2010a**). "Passive spatial mapping of inertial cavitation during HIFU exposure," IEEE Trans. Biomed. Eng. **57**, 48–56.

Gyöngy, M., and Coussios, C.-C. (**2010b**). "Passive cavitation mapping for localization and tracking of bubble dynamics," J. Acoust. Soc. Am. **128**, EL175—EL180.

Hitchcock, K. E., Ivancevich, N. M., Haworth, K. J., Caudell Stamper, D. N., Vela, D. C., Sutton, J. T., Pyne-Geithman, G. J., and Holland, C. K. (**2011**). "Ultrasound-enhanced rt-PA thrombolysis in an ex vivo porcine carotid artery model," Ultrasound Med. Biol. **37**, 1240–1251.

Hudson, J. M., Karshafian, R., and Burns, P. N. (**2009**). "Quantification of flow using ultrasound and microbubbles: A disruption replenishment model based on physical principles," Ultrasound Med. Biol. **35**, 2007–2020.

Hudson, J. M., Williams, R., Lloyd, B., Atri, M., Kim, T. K., Bjarnason, G., and Burns, P. N. (**2011**). "Improved flow measurement using microbubble contrast agents and disruption-replenishment: Clinical application to tumour monitoring," Ultrasound Med. Biol. **37**, 1210–1221.

Hynynen, K., McDannold, N., Vykhodtseva, N., and Jolesz, F. A. (**2001**). "Noninvasive MR imaging-guided focal opening of the blood-brain barrier in rabbits," Radiology **220**, 640–646.

Jensen, C. R., Ritchie, R. W., Gyöngy, M., Collin, J. R. T., Leslie, T., and Coussios, C.-C. (**2012**). "Spatiotemporal monitoring of high-intensity focused ultrasound therapy with passive acoustic mapping," Radiology **262**, 252–261.

Marmottant, P., and Hilgenfeldt, S. (**2003**). "Controlled vesicle deformation and lysis by single oscillating bubbles," Nature **423**, 153–156.

McDannold, N., Vykhodtseva, N., and Hynynen, K. (**2006**). "Targeted disruption of the blood–brain barrier with focused ultrasound: Association with cavitation activity," Phys. Med. Biol. **51**, 793–807.

Poliachik, S. L., Chandler, W. L., Mourad, P. D., Ollos, R. J., and Crum, L. A. (**2001**). "Activation, aggregation and adhesion of platelets exposed to high-intensity focused ultrasound," Ultrasound Med. Biol. **27**, 1567–1576.

Qin, S., and Ferrara, K. W. (**2006**). "Acoustic response of compliable microvessels containing ultrasound contrast agents," Phys. Med. Biol. **51**, 5065–5088.

Qin, S., and Ferrara, K. W. (**2010**). "A model for the dynamics of ultrasound contrast agents in vivo," J. Acoust. Soc. Am. **128**, 1511–1521.

Rifai, B., Arvanitis, C. D., Bazan-Peregrino, M., and Coussios, C.-C. (**2010**). "Cavitation-enhanced delivery of macromolecules into an obstructed vessel," J. Acoust. Soc. Am. **128**, EL310–EL315.

Samuel, S., Cooper, M. A., Bull, J. L., Fowlkes, J. B., and Miller, D. L. (**2009a**). "An ex vivo study of the correlation between acoustic emission and microvascular damage," Ultrasound Med. Biol. **35**, 1574–1586.

Samuel, S., Fowlkes, J., and Miller, D. (**2009b**). "An in vitro study of the correlation between bubble distribution, acoustic emission, and cell damage by contrast ultrasound," IEEE Trans. Ultrason. Ferroelectr. Freq. Control **56**, 589–599.

Sassaroli, E., and Hynynen, K. (**2007**). "Cavitation threshold of microbubbles in gel tunnels by focused ultrasound," Ultrasound Med. Biol. **33**, 1651–1660.

Tung, Y.-S., Choi, J. J., Baseri, B., and Konofagou, E. E. (**2010a**). "Identifying the inertial cavitation threshold and skull effects in a vessel phantom using focused ultrasound and microbubbles," Ultrasound Med. Biol. **36**, 840–852.

Tung, Y.-S., Vlachos, F., Choi, J. J., Deffieux, T., Selert, K., and Konofagou, E. E. (**2010b**). "In vivo transcranial cavitation threshold detection during ultrasound-induced blood-brain barrier opening in mice," Phys. Med. Biol. **55**, 6141–6155.

Wei, K., Jayaweera, A. R., Firoozan, S., Linka, A., Skyba, D. M., and Kaul, S. (**1998**). "Quantification of myocardial blood flow with ultrasound-induced destruction of microbubbles administered as a constant venous infusion," Circulation **97**, 473–483.